

CATALYTIC AND BIOLOGICAL SENSITIVITY OF TiO₂ AND SiO₂ MATRICES WITH SILVER NANOPARTICLES CREATED BY ION IMPLANTATION: A REVIEW

A.L. Stepanov^{1,2}, X. Xiao³, F. Ren³, T. Kavetsky⁴ and Y.N. Osin²

¹Kazan Physical-Technical Institute, Russian Academy of Sciences, 420029 Kazan, Russian Federation

²Kazan Federal University, 420018 Kazan, Russian Federation

³Wuhan University, 430072 Wuhan, China

⁴Drohobych Ivan Franko State Pedagogical University, 82100 Drohobych, Ukraine

Received: May 13, 2013

Abstract. The ion implantation of oxide materials such as TiO₂ and SiO₂ to form silver nanoparticles for catalyst and antibacterial applications is observed. For these purposes the implantation was used at high ion doses that is essential for silver nanoparticle nucleation and grow. It is considered how implanted silver nanoparticles can modify various oxide materials in dependence of irradiation conditions such as ion dose, energy, current density and so on. Some examples of various chemical catalytic and antibacterial reactions in samples with nanoparticles Ag:TiO₂ and Ag:SiO₂ are also presented and discussed. It is demonstrated that ion implantation is one of effective perspective modern techniques for fabrication catalyst and biology-active materials with silver nanoparticles.

1. INTRODUCTION

In general the development of artificial biomaterials is a complicated process. It was recognized that an ideal biomaterial should possess mechanical properties matched with injured tissues for stress-strain balance, establish strong chemical bondings at the biomaterials-tissues interface to ensure artificial material anchorage and exhibit high antibacterial activities to prevent bacterial infection. All of these desirable properties of biomaterials are closely related to overall implant efficacy and can be regulated and tuned by physic-chemical characteristics of biomaterials, such as bulk and surface properties.

Surface modification can be carried out by a lot of methods usually classified as mechanical machining, chemical and physical treatments. Ion implantations, which are proven to be economic and

effective, have already been widely applied in the modification of semiconductors, dielectrics, polymers and biomedical industry. The unique advantage of ion beam modification over the other methods is the ability of selectively enhancing surface properties (approx. several hundred nanometres), whereas the bulk contributions remain unchanged. Another major advantage of ion implantation is the omnidirectional processing capability to tailor the surface properties of many biomaterials by introducing a myriad of different kinds of elements (practically silver ions) and functional groups into the materials with complex shapes. This technique is usually applied in areas such as microelectronics, aerospace engineering and precision manufacturing. Applications of ion implantation technique in biomedical implant modification have attracted increasing interest because of its controllability and versatility.

Corresponding author: A.L. Stepanov, e-mail: aanstep@gmail.com

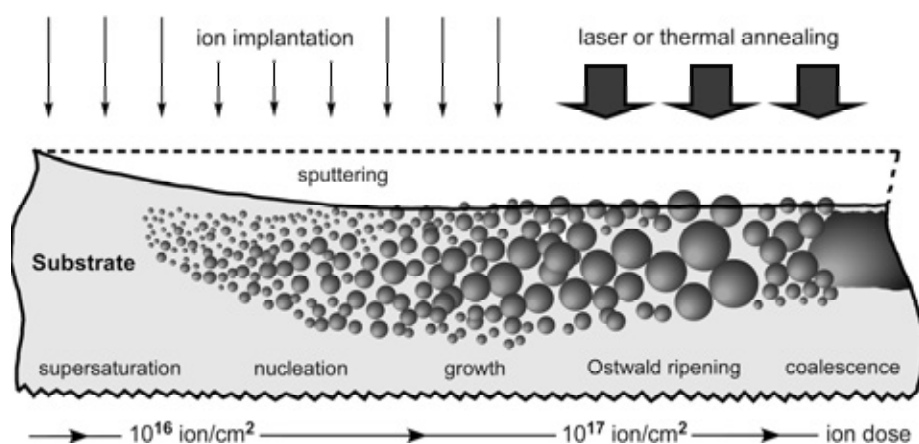


Fig. 1. Basic physical processes (from left to right) involved in the formation of nanoparticle from an implant vs. the ion dose with regard to surface sputtering under irradiation.

It is well known that silver possesses outstanding antibacterial properties in comparison with other heavy metal ions. Therefore, more and more investigations are being made on the antibacterial activity of silver nanoparticles. There are various ways to fabricate antibacterial materials containing silver, but it is a strong challenge to prepare nanoparticles of silver stable enough to significantly inhibit bacterial growth. Ion implantation is an effective method to incorporate antibacterial Ag into the near surface of various dielectrics and semiconductors. This method can be used to meet requirements of antibacterial silica glass in important places, such as hospital surgery rooms, pharmaceutical companies, food shops, and even refrigerator glass, architectural glass, railway stations which are exposed to high risks of bacteria in our daily life.

Also semiconductor photocatalysts were recently attracted considerable attention for advanced oxidation processes used in decontamination, purification and deodorization of air, water and industrial effluents. In this context, TiO_2 is one of the most studied materials thanks to its stability and photosensitivity. Many researchers have investigated on ion implantation into TiO_2 and many fundamental results in physical interest were reported on damage recovery and on lattice site occupation of ion-implanted TiO_2 . A significant amount of research on TiO_2 was performed over the last decades and a number of reviews on various aspects of TiO_2 were published. To enhance the quality of TiO_2 , many producing methods were proposed to dope (or incorporate) trace impurity into TiO_2 . Most of the promising technology for modification and improvement of TiO_2 properties by synthesis of silver nanoparticles is also ion implantation because it allows reaching a high

impurity filling factor in an irradiated matrix beyond the equilibrium limit of impurity solubility. At the same time, this technique provides controllable synthesis of metal nanoparticles at various depths under the substrate surface. This method allows for strict control of the doping ion beam position on the sample surface with implant dose as, for example, in the case of electron- and ion-beam lithography.

In the present review, recent advantages and some examples on application of ion implantation for modification of TiO_2 and SiO_2 to form silver nanoparticles for catalyst and antibacterial applications are presented and discussed together with new original data.

2. ION IMPLANTATION SYNTHESIS OF METAL NANOPARTICLES

Ion implantation is an effective technological tool by which different ions are accelerated in an electrical field and impacted into the surface layer of the substrate to a depth of several micrometers [1,2]. The degree of surface modification of the materials depends on their individual chemical and structural properties, as well as on variations of implantation parameters, such as the type and energy of an implant, current density in ion beam, substrate temperature. A most critical parameter is ion dose F_0 , which determines the implant amount. Depending on the modification of materials, such as, for example, TiO_2 or SiO_2 , by irradiation, ion implantation can be conventionally divided into low-dose and high-dose processes [3,4].

In the case of low-dose irradiation ($\sim F_0 \leq 5.0 \cdot 10^{14}$ ion/cm²), the metal ions implanted, after stopping and thermalization, are dispersed throughout the volume of the dielectrics and are well separated from

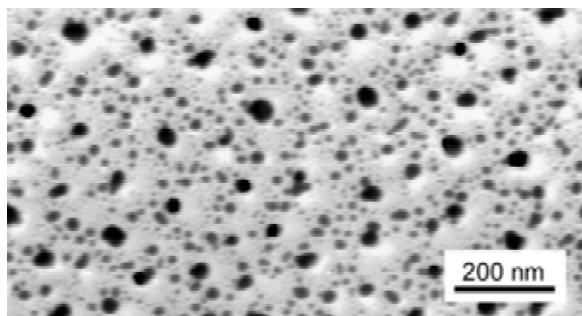


Fig. 2. Micrograph of silver nanoparticles produced by 30-keV Ag^+ implantation into polymethylmethacrylate at a dose of $5.0 \cdot 10^{16}$ ion/cm².

each other. The energy of the implant is transferred to the matrix via electron shell excitation (ionization) and nuclear collisions. This causes radiation-induced defects, which, in turn, may reversibly or irreversibly modify the material structure [1]. Various types of crystal structure damage have been observed in practice: extended and point defects, amorphization and local crystallization, precipitation of a new phase made up of host atoms or implanted ions, etc.

The range of high-dose implantation may be divided into two characteristic dose sub-ranges (Fig. 1) [4]. In the sub-range $10^{15} \leq F_0 \leq 10^{17}$ ion/cm², the concentration of metal and semiconductor ions exceeds the solubility limit of metal atoms in matrices and the system relaxes by nucleation and growth of Nanoparticles as illustrated, for example, in Ag-irradiated polymethylmethacrylate (Fig. 2).

The threshold dose value (at which MNPs nucleate) depends on the type of the dielectric matrix and implant. For example, for 25-keV Ag^+ ion implantation into $LiNbO_3$, the threshold dose was found to be $F_0 \sim 5.0 \cdot 10^{15}$ ion/cm² [5], for 30-keV silver ions embedded in epoxy resin, $F_0 \sim 10^{16}$ ion/cm² [6]. The next sub-range of high-dose implantation, $\sim F_0 \geq 10^{17}$ ion/cm², leads to the coalescence of already existing Nanoparticles with the formation of either MNP aggregates or thin quasi-continuous films at the dielectric surface. For instance, the irradiation of silicone polymer-glass by 30-keV Ag ions at higher-than threshold-nucleation doses favors the formation of aggregate structures. The MNP distribution established in the dielectrics after coalescence or Ostwald ripening may be dramatically disturbed by post-implantation thermal or laser annealing.

The composite materials considered in this review were aimed at studying consisting of isolated MNanoparticles; i.e., the particles were synthesized by high-dose ion implantation ($F_0 \leq 10^{17}$ ion/cm²).

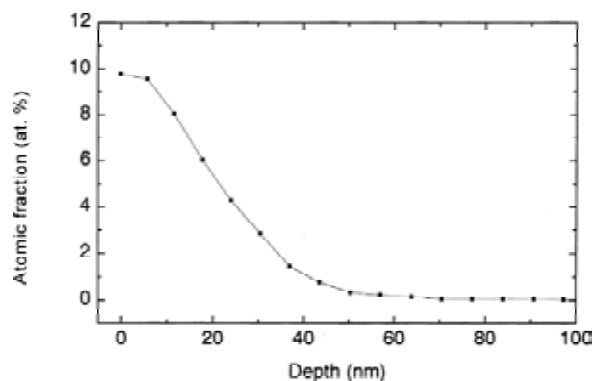


Fig. 3. The depth distribution of silver derived from the RBS spectrum for ion implantation with a dose of $7 \cdot 10^{16}$ ion/cm² and an energy of 60 keV into the silicate glass.

The low energy implantation of metal ions leads to their non-uniform distribution in the depth of the dielectrics, which is different from the Gaussian profile traditionally predicted by statistical theory, primarily because of the effective atom sputtering from the substrate surface during the irradiation. For instance, in Fig. 3 the silver depth concentration in the Ag-implanted soda-lime silicate glass derived from experimental Rutherford backscattering spectrometry (RBS) patterning shows a maximum near the implanted surface of the sample with a penetration to about 60-65 nm [7].

This characterizes the implanted sample as a depth non-uniform metal-insulator object. An excess of metal atoms in the glass, above the solubility limit, causes nucleation of the nanoparticles. As usually the size distribution of nanoparticles appears in the plane of the sample. Additional to this distribution for the implanted sample there is distribution particles in the depth. Since the increase of metal concentration in the depth profile and the sputtering yield depend on implantation time (ion dose), then the MNP nucleation and growth will also vary with time and depth. It is obvious that during the implantation the size of the particles with depth

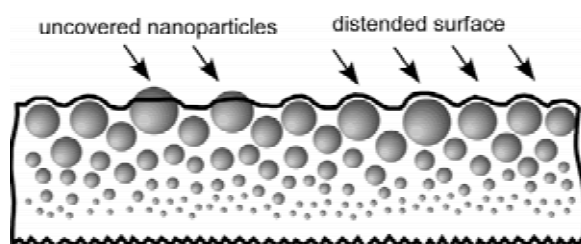


Fig. 4. Schematic illustration of the effects of swelling and stripping as a result of sputtering occurring during the low-energy high-dose ion implantation of dielectric by metal ions.

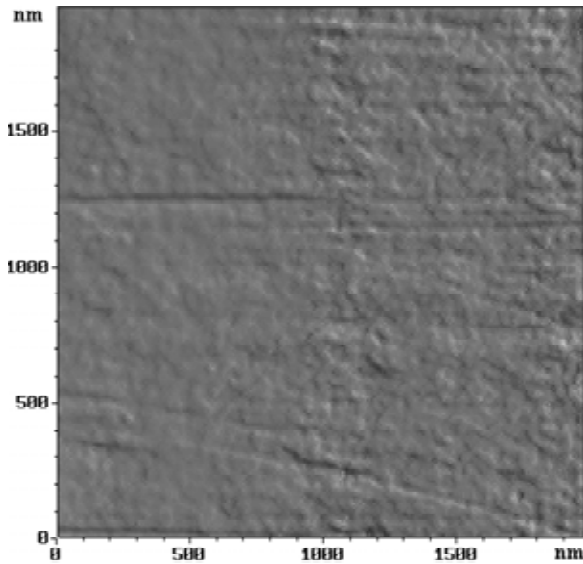


Fig. 5. An AFM image as a top view of the surface of virgin silicate glass.

is “proportional” to the metal filling factor, because they are both determined by the ion concentration profile. Consequently, according to the Figure 3 the large silver nanoparticles in the glass are close to the implanted surface with small ones in the interior of the implant zone (Fig. 4).

The atomic force microscope (AFM) images of the non-implanted and implanted surfaces of the samples are shown in Figs. 5 and 6 [8]. As seen from these figures, compared with the initial glass, the implanted surface is smoother (roughness) that is typical for irradiated glasses at similar conditions. At the same time, there are many hemispherical hills on this surface with an average diameter of approximately 100-150 nm. There are no such protrusions on the unimplanted sample. The reason for the existence of surface hills is assumed to be from a sputtering of irradiated glass during implantation, which leads to unequal ejection of ions of different elements from the surface, exposing the synthesized nanoparticles in the sub-surface glass (Fig. 4).

It was shown in the work [9] silver nanoparticles with the SPR in rutile an sol-gel TiO_2 films can be formed with low-energy ion implantation at the higher doses. Silver negative ions were implanted to TiO_2 by using a negative ion implanter with an RF plasma-sputter-type heavy negative ion source. Mass-separated ^{107}Ag negative ions were implanted at 65 keV. The dose amount was changed from $3 \cdot 10^{16}$ to 10^{17} ions/cm². The ion beam was in size 8 mm in diameter with current density of about $2 \mu\text{A}/\text{cm}^2$.

Optical absorption properties measured for Ag-implanted rutile samples are shown in Fig. 7. All

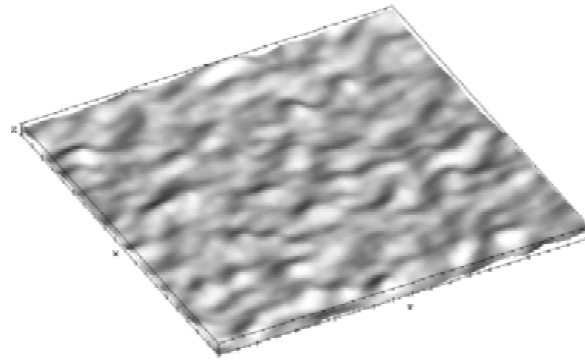


Fig. 6. An AFM image as a top view under lateral illumination of the surface of silicate glass Ag-implanted with a dose of $7 \cdot 10^{16}$ ion/cm² and an energy of 60 keV. The step along the X and Y axes is 100 nm, and the step along the Z axis is 3 nm.

Ag-implanted rutile samples showed absorption peak near 2.6 eV, while the background optical density in whole range of 1.5 - 3 eV was apparently increased with increase in dose. The background absorption is considered to be due to implantation damage. The absorption peaks for Ag-implanted rutile were different in peak position from the predicted calculated SPR absorption peak. Two main reasons are considered in decrease of refraction index and oxidation of Ag nanoparticles. The increase in background absorption as increasing in dose showed that many defects and voids resulted in the rutile. Therefore, the refraction index of the matrix around nanoparticles might be smaller than original rutile, so that absorption peak of SPR was shifted to position of higher photon energy. When the refraction index is $n = 2.0$, the peak position was calculated to be about 2.6 eV. However, this

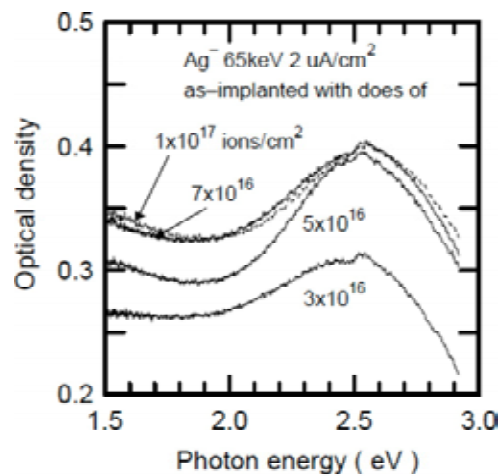


Fig. 7. Optical density spectra of Ag-implanted rutile samples as-implanted with various dose amount. Adapted from [9].

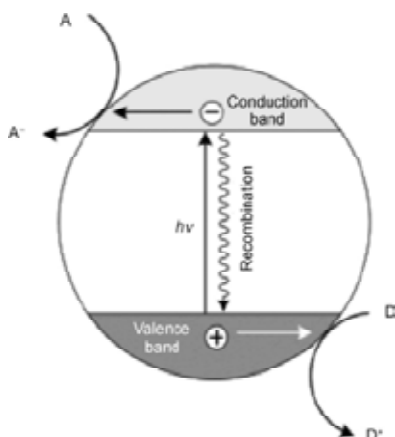


Fig. 8. Mechanism of light absorption by TiO_2 . Adapted from [10].

change in refraction index will be too large. Another reason of the peak shift of SPR is the formation of alloy or partially oxide nanoparticles.

3. PHOTOCATALYSTS ACTIVITY

3.1. Photoproperties of titanium oxide

When TiO_2 is exposed to near-UV light, electrons in the valence band are excited to the conduction band leaving behind holes (h^+), as shown in Fig. 8. The excited electrons (e^-) in the conduction band are now in a purely 3d state and because of dissimilar parity, the transition probability of e^- to the valence band decreases, leading to a reduction in the probability of e^-/h^+ recombination [10].

Anatase TiO_2 is considered to be the active photocatalytic component based on charge carrier dynamics, chemical properties and the activity of photocatalytic degradation of organic compounds. It has inherent surface band bending that forms spontaneously in a deeper region with a steeper potential compared with the rutile phase (Fig. 9) [10] thus surface hole trapping dominates because

spatial charge separation is achieved by the transfer of photogenerated holes towards the surface of the particle via the strong upward band bending. However, in the rutile phase, the bulk recombination of electrons and holes occurs, so only holes very close to the surface are trapped and transferred to the surface.

As was mentioned in the work [10] TiO_2 represents an effective photocatalyst for water and air purification and for self-cleaning surfaces. Additionally, it can be used as antibacterial agent because of strong oxidation activity and superhydrophilicity. TiO_2 shows relatively high reactivity and chemical stability under ultraviolet light ($\lambda < 387$ nm). The development of photocatalysts exhibiting high reactivity under visible light ($\lambda > 400$ nm) should allow the main part of the solar spectrum, even under poor illumination of interior lighting, to be used.

The photocatalytic mechanism in TiO_2 is initiated by the absorption of the photon $h\nu_1$ with energy equal to or greater than the band gap of TiO_2 (~ 3.3 eV for the anatase phase) producing an electron-hole pair on the surface of TiO_2 as schematized in Fig. 10. An electron is promoted to the conduction band (CB) while a positive hole is formed in the valence band (VB). Excited-state electrons and holes can recombine and dissipate the input energy as heat, get trapped in metastable surface states, or react with electron donors and electron acceptors adsorbed on the semiconductor surface or within the surrounding electrical double layer of the TiO_2 . After reaction with water, these holes can produce hydroxyl radicals with high redox oxidizing potential [10]. Depending upon the exact conditions, the holes, OH radicals, O_2^- , H_2O_2 , and O_2 itself can play important roles in the photocatalytic reaction mechanism.

The visible light photoactivity of metal-doped TiO_2 can be explained by a new energy level produced in

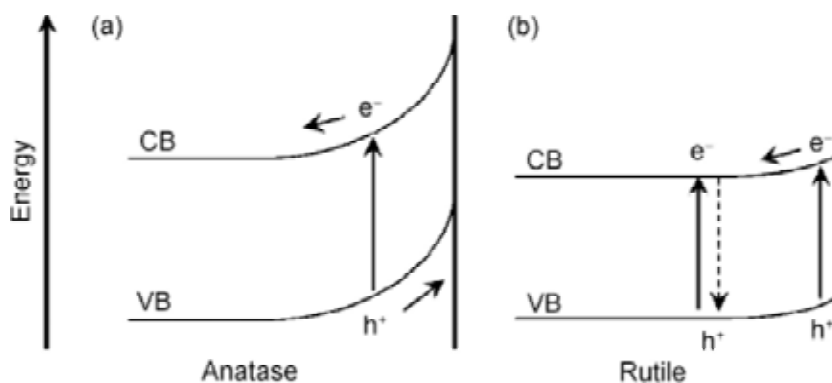


Fig. 9. Surface band bending of the anatase (a) and rutile phases of TiO_2 (b). Adapted from [10].

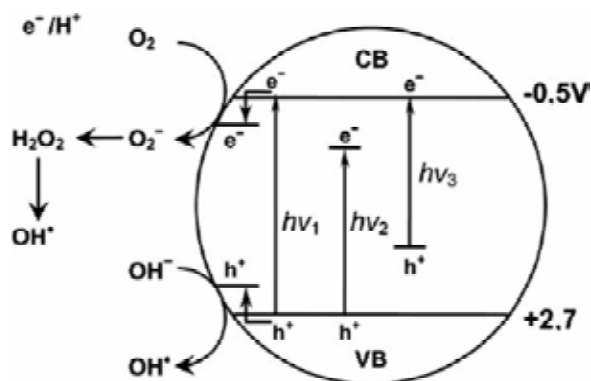


Fig. 10. Mechanism of TiO_2 photocatalysis: $h\nu_1$: pure TiO_2 ; $h\nu_2$: metal-doped TiO_2 and $h\nu_3$: nonmetal-doped TiO_2 . Adapted from [10].

the band gap of TiO_2 by the dispersion of metal nanoparticles in the TiO_2 matrix. As shown in Fig. 10 electron can be excited from the defect state to the TiO_2 conduction band by photon with energy equals $h\nu_2$. Additional benefit of metal doping is the improved trapping of electrons to inhibit electron-hole recombination during irradiation. Decrease of charge carriers recombination results in enhanced photoactivity.

There are three different main opinions regarding general modification mechanism of TiO_2 doped with nonmetals [10]. (1) Band gap narrowing; (2) Impurity energy levels; and (3) Oxygen vacancies. 1. Band gap narrowing: it was found that N $2p$ state hybrids with O $2p$ states in anatase TiO_2 doped with nitrogen because their energies are very close, and thus the band gap of N: TiO_2 is narrowed and able to absorb visible light. 2. Impurity energy level: it was stated that TiO_2 oxygen sites substituted by nitrogen atom form isolated impurity energy levels above the valence band. Irradiation with UV light excites electrons in both the VB and the impurity energy levels, but illumination with visible light only excites

electrons in the impurity energy level. 3. Oxygen vacancies: it was concluded that oxygen-deficient sites formed in the grain boundaries are important to emerge vis-activity and nitrogen doped in part of oxygen-deficient sites are important as a blocker for reoxidation.

3.2. Photoactivity of titanium oxide with silver nanoparticle

Recently, study reveals noble metal nanoparticles, such as Ag, can also improve the photoresponse property of TiO_2 in the visible region based on the SPR effect [11-13]. It is known that the free electrons of metal can collectively oscillate induced by light irradiation, when the oscillation frequency of light electromagnetic field is in accordance with the free electrons, the SPR effect generates and light energy is coupled into the metal nanoparticles in the meantime. Fig. 11 shows the rough schematic of photocatalytic water splitting by Ag/ TiO_2 based on the SPR effect [14]. Electrons are excited from valence band to conduction band in TiO_2 by UV light, and then migrate to Ag nanoparticles (Ag Nanoparticles). The SPR effect induced by appropriate visible light can boost the energy of trapped electrons, resulting in photocatalytic activity enhancement.

In the work [15] authors fabricated plasmonic photocatalyst Ag/AgCl/ TiO_2 nanotubes, which exhibited a highly photocatalytic activity on methylene orange degradation, arising from SPR effect of Ag Nanoparticles under visible light irradiation. Also TiO_2 nanotubes loaded with Ag Nanoparticles were prepared by microwave-assisted chemical reduction method [14]. The experiment of methylene blue (MB) photodegradation was conducted to investigate the SPR phenomenon. The

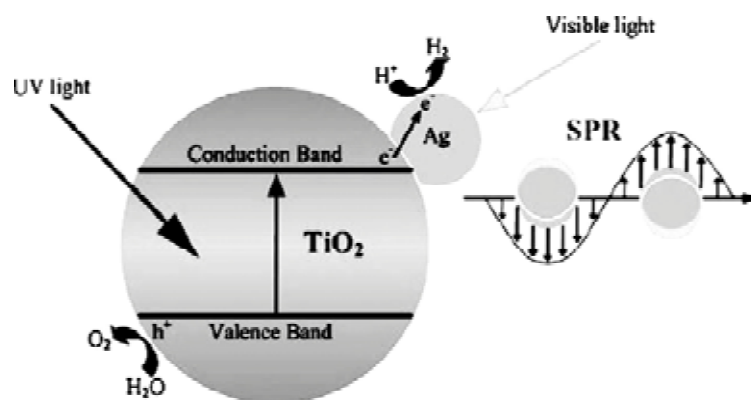


Fig. 11. Schematic diagram of photocatalytic water splitting by Ag/ TiO_2 based on the SPR effect. Adapted from [14].

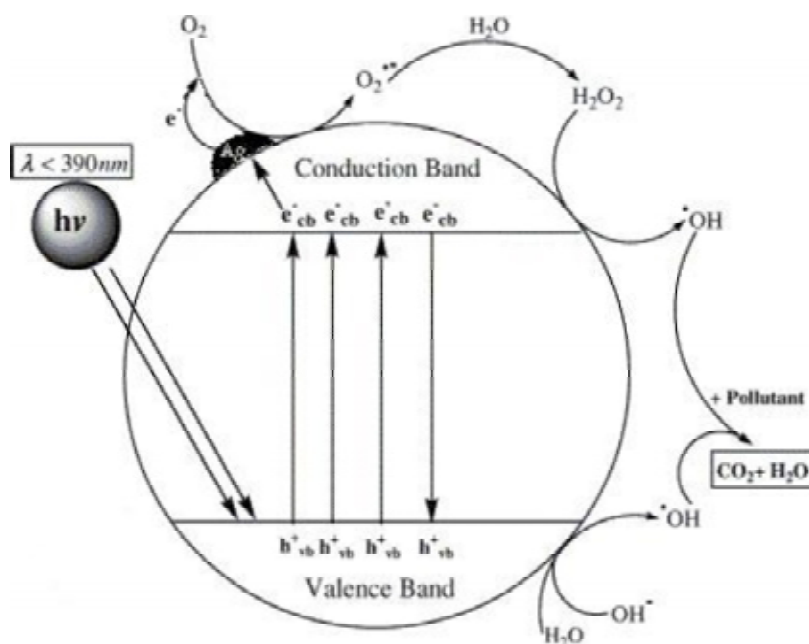


Fig. 12. Mechanism of photocatalyst in Ag deposited TiO_2 powder. Adapted from [17].

photocatalytic performance was evaluated by photocatalytic water splitting.

TiO_2 -supported silver nanoparticles were utilized as a highly efficient catalyst for the addition of terminal alkynes to aldehydes to prepare propargylic alcohols with the promotion by triphenylphosphine [16]. Both a significant support effect and a ligand effect were observed in the catalytic reaction. With this protocol, various propargylic alcohol derivatives were synthesized from aldehydes and terminal alkynes in good to excellent yields. Furthermore, the catalyst could be recovered and reused effectively without obvious reduction in catalytic activity.

Silver doped TiO_2 nanoparticles were studied in the work [17]. The photocatalytic activity was tested by photocatalytic degradation of C.I. Acid Red 88 (AR88) as a model compound from monoazo textile dyes. Results show silver doped TiO_2 is more efficient than undoped TiO_2 at photocatalytic degradation of AR88. The positive effect of silver on

the photoactivity of TiO_2 at degradation of AR88 may be explained by its ability to trap electrons. This process reduces the recombination of light generated electron-hole pairs at TiO_2 surface. Also it was observed reversely Ag- TiO_2 system, the superoxide anion radical is formed as a result of oxygen reduction by transfer of trapped electrons from Ag metal to oxygen, as can be seen in Fig. 12.

The efforts to explore SPR effect to induce charge separation efficiencies in photocatalytic systems Ag/ TiO_2 often undermine the electron acceptor properties of metal nanoparticles. The results presented in the work [18] demonstrate that photocatalytically deposited Ag on TiO_2 nanoparticles improves the photoelectrochemical performance of the Ag/ TiO_2 composite by capturing the photogenerated electrons and maintaining a more negative Fermi level. The shift in the SPR of Ag shows that the charge equilibration between TiO_2 and Ag is dependent on the irradiation conditions. The charging and discharging can be reversibly modulated through

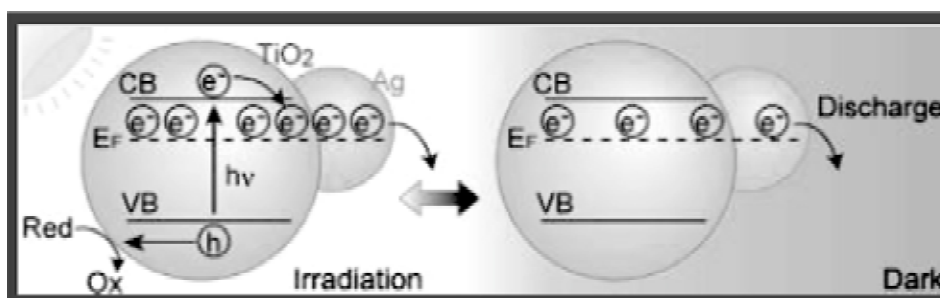


Fig. 13. Charge equilibrium scenarios between TiO_2 and Ag nanoparticles during continuous UV irradiation and in the dark. Adapted from [18].

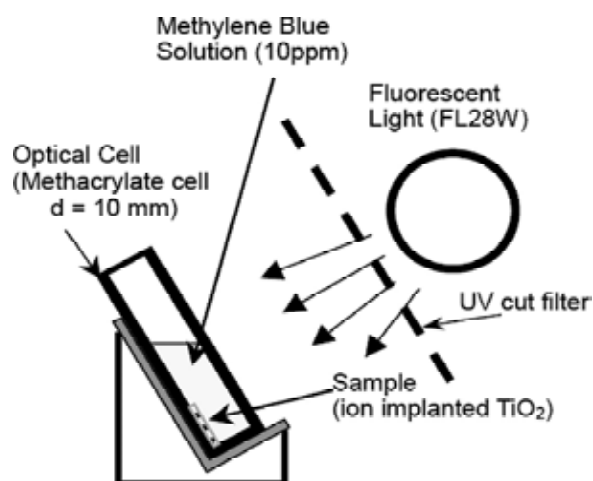


Fig. 14. Schematic configuration of decolorization test. Adapted from [9].

on-off cycles of UV irradiation (Fig. 13). These electron storage effects should be taken into consideration while evaluating the photocatalytic and photoelectrochemical properties of semiconductor/metal composites.

3.3. titanium oxide with implanted silver nanoparticles

For an application in a room illuminated by fluorescent light or incandescent lamp, the photocatalytic performance of TiO_2 should be improved, i.e. high efficiency and activation by visible light, because the light has few components of ultraviolet (UV) light. In the work [9] photocatalytic properties of Ag-ion implanted rutile TiO_2 were studied to show metal nanoparticle formation in the surface region and improvement of photocatalytic efficiency. For these purposes ion implantation of crystalline TiO_2 at 65 keV with doses ranged from $3 \cdot 10^{16}$ to 10^{17} ion/cm² were performed. Some samples were annealed after implantation.

As evaluation of photocatalytic efficiency, decolorization method of methylene-blue (MB) solution with implanted samples under irradiation of a fluorescent light was applied (Fig. 14). In the experimental set up, each of implanted and unimplanted rutile samples was put in individual methacrylate optical cell (optical distance 10 mm, Fisher) with MB solution (10 ppm, 2 ml). The optical cells with implanted and original rutile as well as the cell without any rutile were covered to avoid evaporation of water, and were irradiated with fluorescent light ($2.7 \mu\text{W}/\text{cm}^2$ in ultra violet light) in a dark box. The temperature of the box was about 22 °C. Optical densities of the pale methylene-blue solution in the optical cell were measured at

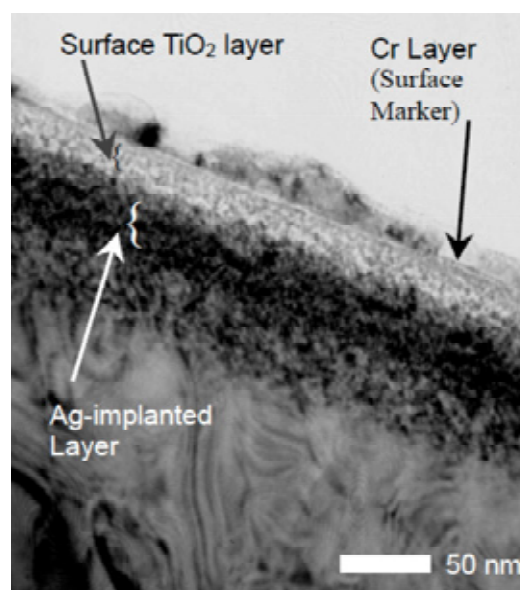


Fig. 15. Cross-sectional TEM micrograph of the Ag-implanted rutile at conditions of 65 keV, $5 \cdot 10^{16}$ ions/cm² at normal, 300°C annealed. Adapted from [9].

photon energy of 1.88 eV (659 nm), at which methylene blue solution has a characteristic absorption peak. The solution was decolorized even without rutile by light irradiation. Photocatalytic efficiencies of the ion-implanted rutile against that of unimplanted rutile were calculated from optical densities taking accounts of difference in area of rutile and also of difference in optical density without any rutile. A UV cut filter with cut-off wavelength of 420 nm (2.95 eV) for evaluation without any ultra violet light was used.

Formation of Ag nanoparticles in TiO_2 after implantation was evidenced by appearance of SPR absorption in visible spectra (Fig. 7). The background absorption is considered to be due to implantation damage. The increase in background absorption as increasing in dose showed that many defects and voids resulted in the rutile. After annealing some reduction of background was detected. The result of a cross-sectional TEM observation is shown in Fig. 15, where very small Ag nanoparticles of about 1 nm in diameter was appeared in the surface layer.

Photocatalytic efficiencies in decolorization of methylene-blue for the metal-implanted samples at annealing temperature are shown in Fig. 16, where relative efficiencies were normalized by that of unimplanted rutile. The as-implanted and annealed samples at below 300 °C showed worse photocatalytic properties than the original rutile. The Ag-implanted rutile with $3 \cdot 10^{16}$ ions/cm² had the best efficiency of 2.2 after annealing at 500 °C.

Damages and defects in rutile play as recombination center of activated electron and hole. Dete-

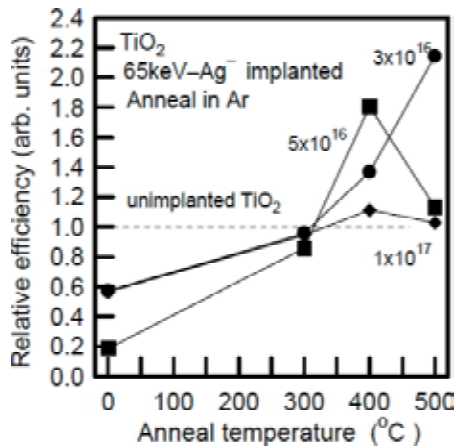


Fig. 16. Relative photocatalytic efficiency of Ag-implanted rutiles in decolorization test of methylene blue solution under irradiation of fluorescent light, where the relative efficiency is normalized by the photocatalytic efficiency of the unimplanted rutile. Adapted from [9].

rioration of photocatalytic property in as-implanted and at low annealing temperature is due to implantation damage of the surface layer of rutile. The increase in the efficiency more than that of unimplanted rutile is owing to damage recovery and existence of silver nanoparticles. The reason of improving photocatalytic properties by metal nanoparticles is *not understood* in detail [9]. But followings are considered. (1) Noble metals have large electronegativity. Therefore, main reason is that the noble metal nanoparticles play as electron acceptor in the surface layer to decrease recombination of hole and electron. (2) Therefore, visible light with energy less than the activation energy of 3.0 eV may contribute to activate the rutile leading to improvement of photocatalytic performance. (3) Nanoparticles on the rutile surface play as catalysis by themselves because of their very active surfaces. (4) When implanted metal atoms occupy lattice sites of rutile, a doping impurity level is resulted between energy bandgap of rutile to contribute to decreasing photon energy to be required for activation.

In order to maximize the utilization rate of UV region of the sunlight, in our research, we also design a new composite structure to enhance the light absorption efficiency by coupling TiO_2 to Ag nanoparticles embedded in SiO_2 formed by Ag low energy ion implantation. As was mentioned Ag nanoparticles show SPR effects in the near-UV region, which strongly enhances the electric field in the vicinity of nanoparticles. This enhanced electric field at near-UV region could increase the UV light

absorption to boost the excitation of electron-hole pairs in TiO_2 and thus increase the photoelectric conversion efficiency. In such kind of structure, the Ag nanoparticles embedded in SiO_2 serves two purposes. Firstly, SiO_2 is a protective layer prevents Ag to be oxidized through direct contact with TiO_2 . Secondly, the size and depth distributions of the embedded Ag Nanoparticles can be controlled by choosing implantation parameters and post-implantation thermal treatment [4], which can tune the SPR spectrum of Ag nanoparticles to match the absorption edge of TiO_2 . Thus, it is possible to design nanostructures that concentrate the light surrounding near Ag nanoparticles, which enhance the light absorption of TiO_2 film.

To create composites high purity silica slides were implanted by Ag ions from 20 to 60 keV to dose of $5.0 \cdot 10^{16}$ ions/cm² and at 40 keV to $1.0 \cdot 10^{17}$ ions/cm² using a metal vapor vacuum arc ion source implanter. The TiO_2 - SiO_2 -Ag nanostructural structures were obtained by depositing TiO_2 films (100 nm thick) on the surface of the as-implanted silica substrates using direct-current (DC) reactive magnetron sputtering system. Subsequently, all deposited samples were annealed at 500 °C in oxygen gas for 2 hours to obtain anatase phase TiO_2 film. The photocatalytic efficiencies of TiO_2 and TiO_2 - SiO_2 -Ag nanostructural composites with an area of 4 cm² were evaluated by measuring the degradation rates of 5 mg/L methylene blue (MB) solution under UV-vis irradiation. A mercury lamp (250 W with characteristic wavelength at 365 nm) was used as a light source. The TiO_2 and the TiO_2 - SiO_2 -Ag composites films were placed into 40 mL MB solution with a concentration of 5 mg/L. Before irradiation, the samples were put into 40 mL MB solution for 30 minutes in the darkness to reach absorption equilibrium. The decolorization of MB solution was measured by an UV-vis spectrometer at the wavelength of 664.0 nm. The absorption spectrum of the MB solution was measured at a time interval of 30 minutes and the total irradiation time was 4 hours.

Fig. 17 shows the optical absorption spectra of TiO_2 - SiO_2 -Ag and the TiO_2 films. The absorption edge around 390 nm belongs to the intrinsic exciton absorption of TiO_2 [19]. The obvious absorption peaks at about 419-433 nm can be attributed to the SPR absorption of Ag Nanoparticles formed by Ag ion implantation [4,20]. As seen the SPR of Ag nanoparticles is very close to the exciton edge (around 390 nm) of anatase TiO_2 . Therefore, it is expected that an efficient energy transfer from the Ag nanoparticles to TiO_2 can be occurred. The

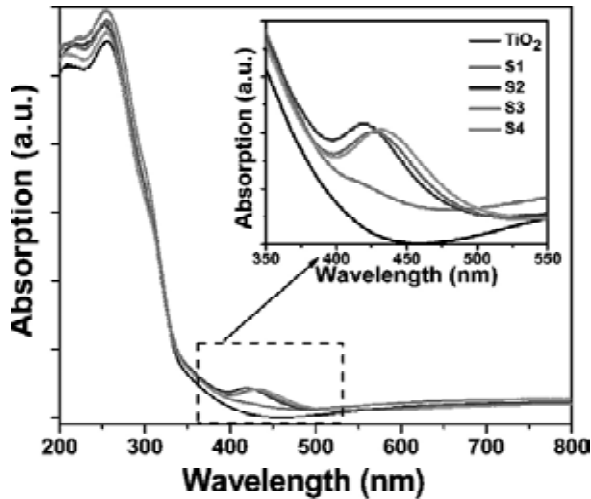


Fig. 17. Optical absorption spectra of virgin TiO_2 and annealed TiO_2 - SiO_2 -Ag, which were ion implanted at various energies (S1) 20; (S2) and (S3) 40; (S4) 60 keV and doses (S1), (S2), (S4) $5.0 \cdot 10^{16}$; (S3) $1.0 \cdot 10^{17}$ ions/cm².

position of Ag SPR absorption peak of the S2 is around 419 nm, which is blue shift comparing to that of the other three samples. The SPR peak of the sample (S2) is the most close to the anatase TiO_2 exciton energy, therefore the strongest resonant coupling effect between Ag SPR and the excitons of the TiO_2 films may be produce more effectively.

To illustrate the strong electromagnetic near field induced by the SPR from Ag nanoparticles, the Raman scattering spectra of S1-S4 and TiO_2 are presented in Fig. 18. The observed Raman bands at 144, 199, 399, 516, and 640 cm^{-1} can be assigned to the Eg, Eg, B1g, A1g, or B1g and an Eg vibration modes of anatase TiO_2 phase, respectively, which are consistent with the characteristic patterns of pure anatase without any trace of rutile or brook-

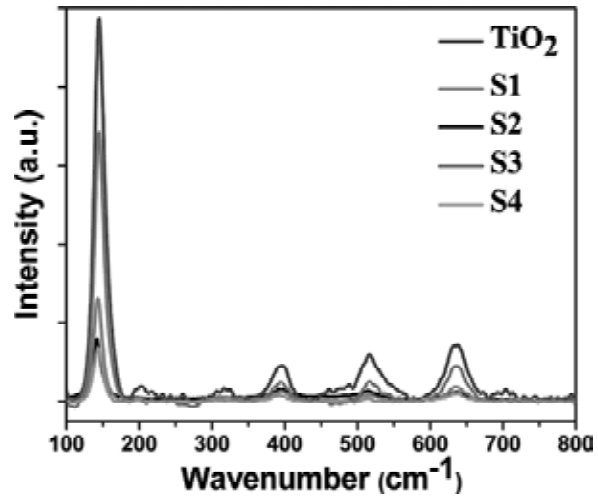


Fig. 18. The Raman scattering spectra of S1-S4 (samples as in Fig. 17) and the pure TiO_2 film.

ite phase [21]. It is seen that the Raman intensity for S1-S4 increase compared to that of TiO_2 , and the S2 shows the strongest Raman intensity. It is well known that Raman scattering intensity is proportional to the electric field intensity [22], thus stronger Raman scattering attained from the TiO_2 - SiO_2 -Ag structure indicates that a stronger electric near field is induced by Ag Nanoparticles embedded in SiO_2 substrate. When the Ag Nanoparticles are irradiated by laser in spectral area of particle absorption band longer wavelength shoulder, a strong near field is produced due to the SPR, so Raman scattering is enhanced. As seen from Fig. 18, the enhancement factors of Raman scattering of S1-S4 is different because of various coupling field efficiency.

The microstructural characterization of the TiO_2 - SiO_2 -Ag (S1-S4) were analysed by TEM (Fig. 19).

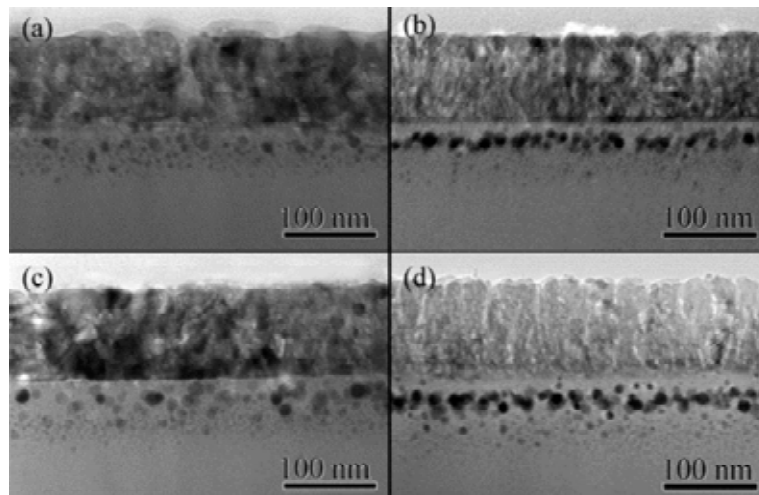


Fig. 19. Cross-sectional TEM images of the (a) S1, (b) S2, (c) S3, (d) S4 (samples as in Fig. 17).

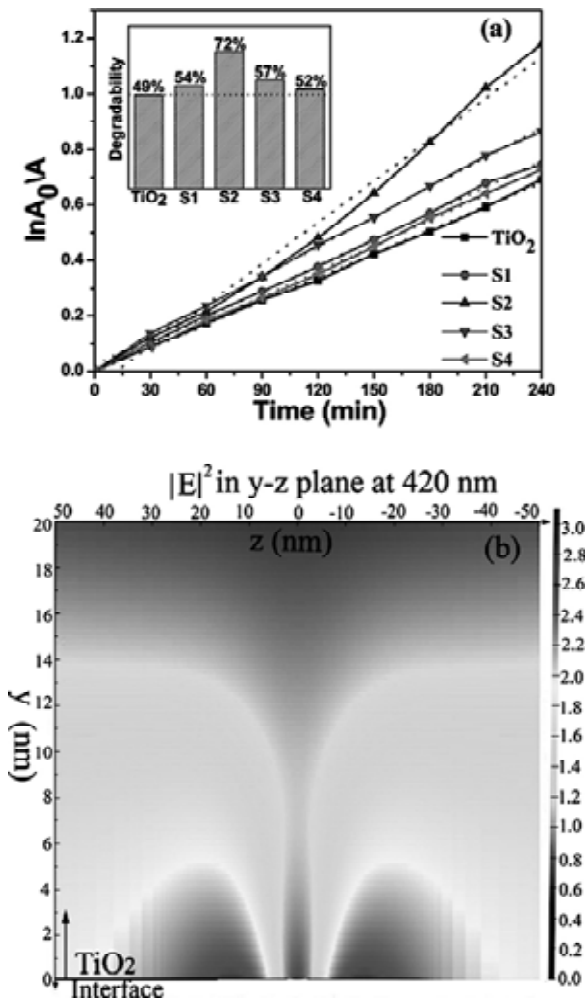


Fig. 20. The photodegradation of MB solution by S1-S4 and reference sample TiO_2 under UV light irradiation (inset one), and corresponding plots of $\ln(A_0/A)$ versus the irradiation time, showing the linear fitting results; (b) amplitude enhancement of electric field inside a TiO_2 layer is simulated by FDTD method (samples as in Fig. 17).

The TEM image of the S1 (Fig. 19a) shows that the size of Ag Nanoparticles appears with widely distributed. However, increasing the implantation energy to 40 keV as shown in Fig. 19b, the Ag Nanoparticles in the S2 are quite uniform in size (with an size of 20 nm) and distribute at nearly the same depth of 7 nm from the surface. Under higher energy ion implantation, more heat will be induced in the sample in short time, which enhances the diffusion of Ag atoms. Therefore, the implanted Ag ions trend to aggregate to larger nanoparticles around the projected range [23]. The near field induced by the SPR of Ag Nanoparticles is strong due to the presence of the formed Ag nanoparticles with bigger size and the near-field dipolar interactions between adjacent particles. On the other hand, the dipolar

interactions between adjacent particles with near the same size can result in a blue shift of SPR [20], thus the blue shift in the SPR peak of Ag nanoparticles observed in the Fig. 17, which may produce a strongest resonant coupling effect between the SPR of Ag nanoparticles and TiO_2 . It means the stronger near field can be induced. In this case, the S2 has the strongest Raman scattering enhancement factor. The size of Ag nanoparticles in the S1 is smaller and the distribution is wide than that in the S2. It means that the near field induced by SPR of Ag Nanoparticles is weaker than that in the S2. Further increasing the implantation energy to 60 keV as presented in Fig. 19d, Ag nanoparticles in the S4 locate deeper into the surface than that of S2.

Since the SPR is an evanescent wave that exponentially decays with distance from the MNP surface [24], the enhancement of Raman scattering decrease progressively with the increase of distance between Ag nanoparticles with the TiO_2 film, therefore Raman scattering intensity of the S4 has almost no enhancement. When the ion implantation dose is increased to $1.0 \cdot 10^{17}$ ions/cm² with implantation energy of 40 keV (S3) as displayed in Fig. 19c, large Ag nanoparticles with size about 15 nm locate near the surface and the small ones in deeper matrix. The surface sputtering effect plays an important role for ion implantation at higher dose, the formed small Ag nanoparticles near the surface are sputtered by the following implanted ions, so the large Ag nanoparticles are near the surface of the S3 [4].

As was mentioned to demonstrate the enhancement of light absorption in TiO_2 - SiO_2 -Ag nanostructural composites, the photocatalysis activities of the S1-S4 are investigated by the UV degradation of MB solution at room temperature. As shown in Fig. 20a inset one, the concentration of MB is decreased upon the irradiation time, and the TiO_2 film can decompose 49% of MB after irradiation for 4 hours. However, the TiO_2 - SiO_2 -Ag nanostructural composite films obtained higher photocatalytic efficiency than the pure TiO_2 film, and the S2 has the highest photocatalytic efficiency than other three samples, and degrade 72% MB. The enhancement ratio is as high as 47%. Meanwhile, the photodegradation of MB can be assumed to follow the classical Langmuir-Hinshelwood (L-H) kinetics [25], and its kinetics can be expressed as follows: $\ln(A_0/A) = kt$, where k is the apparent first-order reaction rate constant (min^{-1}), A_0 and A represent the absorbance before and after irradiation for time t , respectively. As displayed in Fig. 20a, S2 shows

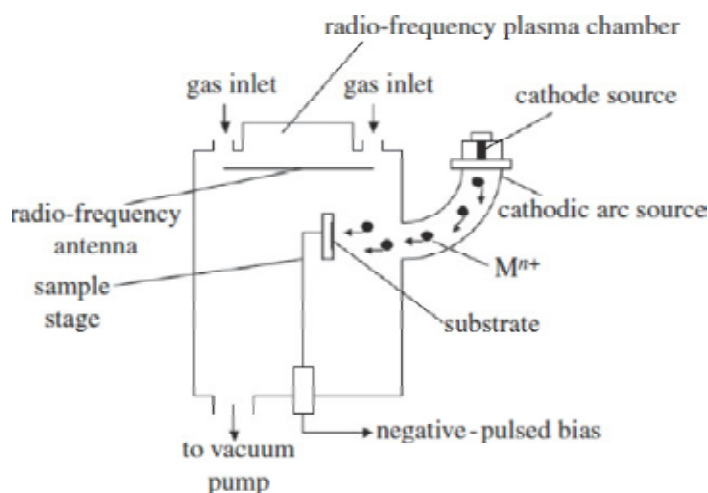


Fig. 21. Schematic of ion implantation and deposition processes. Adapted from [26].

the highest rate constant among all the samples, the k values of the S2 is 2 times higher than that of the pure TiO_2 . The kinetic rate constants follow the order $S2 > S3 > S1 > S4 > \text{TiO}_2$. This is consistent with the Raman scattering enhancement result.

The near field enhancement in the TiO_2 layer due to the presence of the Ag nanoparticles is also simulated by FDTD method as shown in Fig. 20b. In constructed structure, we consider x as the light incident direction, the illuminating plane wave with a wavelength of 420 nm is y polarized, and an Ag nanoparticle with a diameter of 20 nm is embedded in SiO_2 , and the distance to the surface of SiO_2 substrate is 7 nm. An amplitude enhancement to 3 can be observed. Theoretical and experimental results show that an enhancement of near field is induced by the SPR of Ag nanoparticles. The SPR excitations cause a large increase in electromagnetic field in the vicinity of metal Nanoparticles, the localized amplification can increase the incident excitation field and boost the creation of hole-electron pairs, which results in the enhancement of the photocatalytic activity of TiO_2 .

4. BIOACTIVITY OF IMPLANTED SILVER NANOPARTICLES

4.1. Improvement antibacterial activity of biomaterials by ion implantation

In the study [26], recent work on applying plasma immersion ion implantation and deposition (PIID) technique to improve bioactivity, haemocompatibility and antibacterial activity of biomaterials was presented. To produce plasma, electron separation from atoms or molecules in the gas state, or ionization, is required. During the PIID processing, a

workpiece is immersed in plasma under a high bias voltage, which repels electrons away from the workpiece while driving the positive ions of the plasma toward it, creating a plasma sheath around the workpiece. Positive ions will be accelerated by the electric field and implanted vertically into the negative potential surfaces, as illustrated in Fig. 21 [26].

Today, most biomedical devices available in the marketplace are made from titanium and its alloys, stainless steel, polymers and ceramics. Although considerable advances have already been made in improving the biological performances of these biomaterials, the ideal long-term stability is still not achieved.

Bacterial infection has been recognized as a serious problem during implant surgery, which may lead to implant failure, revision surgery and even member amputation, all associated with extremely high medical costs not to mention the pain and suffering of the patients [27]. Although antibiotics are still the main treatments for clinical infections, their widespread abuse has given rise to a breed of super bacteria that are resistant to common antibiotics, which is becoming more severe nowadays [27]. One exciting direction is to fabricate antibacterial biomaterials by incorporating broad-spectra bactericidal agents into surfaces or modifying surface physico-chemical properties to prevent bacterial growth or adhesion.

As well-known broad-spectra antimicrobial agents such as silver was implanted into various materials surfaces using PIID to offer excellent antibacterial activities. Liu's group has recently prepared Ag nanoparticle-embedded Ti-composites via single Ag PIID and proposed a new antibacterial mechanism for Ag-Ti [28]. It is believed that Ag and

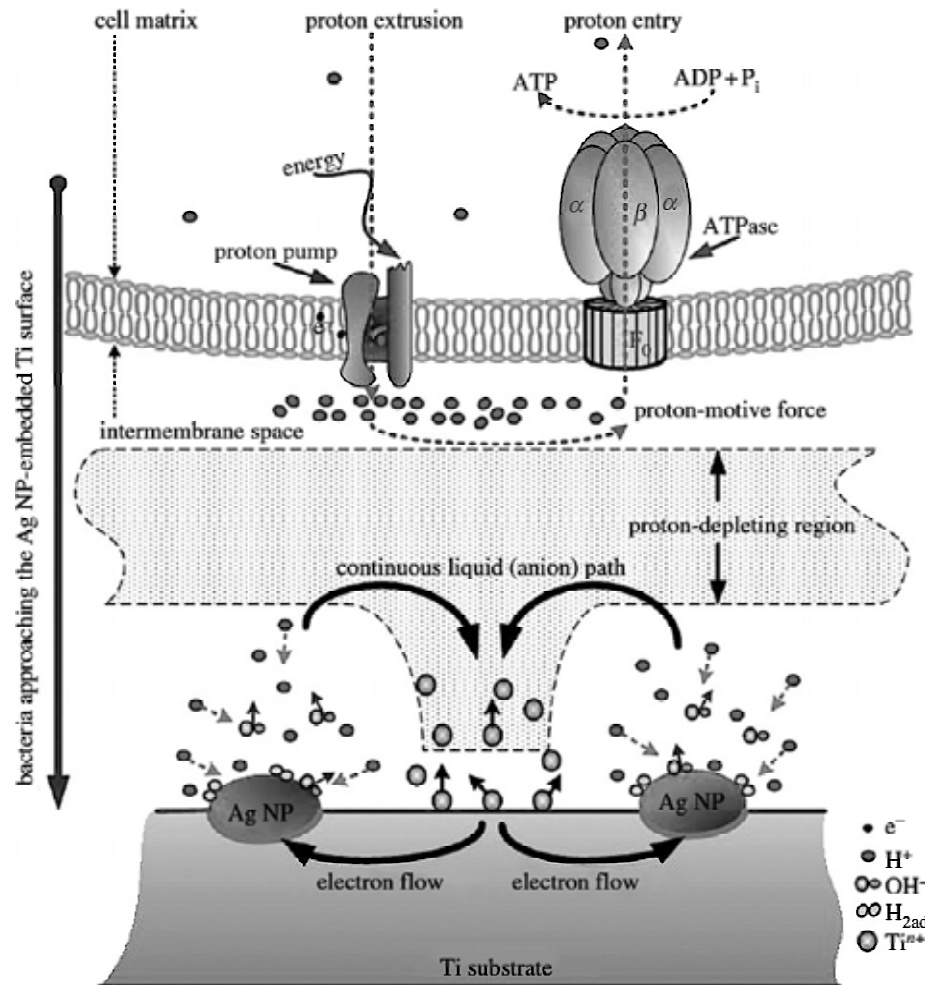


Fig. 22. Illustration for the possible toxicity mechanism on the Ag nanoparticle embedded surface. Adapted from [28].

Ti will constitute one microgalvanic couple owing to the different potentials when immersed in an electrolyte solution. The cathodic reaction will form a proton-depleted region between bacterial membrane and titanium substrate, which probably disrupts the synthesis of adenosine triphosphate and leads to bacteria death. It is notable that proliferation of bacteria is inhibited on the Ag-Ti surface where that of osteoblasts is promoted. The inconsistent results are probably due to the larger size of human cells and the different synthetic and growth mechanisms between bacteria and human cells. Hence, this finding provides important clues on how to achieve specific biological responses to different species on the same surface. The schematic of this proposed mechanism is illustrated in Fig. 22.

4.2. Implanted silver nanoparticles to prevent infection complications

The prevention of medical device related infections remains a main objective because of the still high

rate of complications, leading to hospitalisation and human injury. Such devices generally involve artificial materials in contact with living matter by a surface, which is an easy channel for bacteria proliferation. Polymers are the most commonly used biomaterials due to the compatibility of their viscoelastic properties with human tissues. Efforts to prevent bacterial colonization of these biomaterials have focused on the modification of the polymer surfaces to induce bactericidal properties and preserve at the same time bulk mechanical properties of the device. For this purpose, coatings and surface treatments have been extensively studied and a particular interest was devoted to silver as it combines antimicrobial activity and low human toxicity. Surface engineering techniques involving ion bombardment are particularly interesting to induce new surface properties without altering bulk properties as only a small surface thickness of the material is involved. These ions in polymers can escape from the implanted region through migration to the surface (general case of rare gases) or be stabilized through the formation

of new chemical bonds or precipitation inducing MNPs [3].

In the work [29] authors investigated the efficacy of ion beam techniques to reduce bacterial adhesion/or to induce bactericidal activity of polymer material - poly(ethylene) (PE). For that the implantation of silver, known for its bactericidal action, was used. It was discussed that the biological activity resulted from the formation of metallic colloidal silver near the surface of the polymer, associated to the formation of a dense surface acting as a diffusion barrier. Reduction of the implantation energy to 10 keV, led to activity enhancement resulting from the easier accessibility of surface colloids. Ion beam irradiations were performed from 50 to 10 keV using the Balzers Ion Implanter at room temperature.

Optical absorption spectra of PE films Ag-irradiated with $2 \cdot 10^{16}$ ion/cm² at 15 keV show a strong increase of the absorption in the UV region extending towards the visible spectrum (Fig. 23). Beside the shift of the UV absorption edge, the optical absorption spectrum of PE films implanted with Ag ions exhibits a broad absorption band with a maximum at 550 nm, which can be attributed to colloidal silver at the surface.

Bacterial adhesion tests using *Staphylococcus epidermis* were performed to assess the treatment efficiency to reduce bacteria colonisation. The treated material was evaluated for each test simultaneously with the untreated material for reference. The samples were incubated for 24 h at 30-35 °C and bacteria were counted after elimination of the non adherent bacteria according to a validated extraction protocol. Bactericidal efficiency has been measured through viable bacteria counting in the extract solution of treated samples. Because of the reported loss of silver activity resulting from silver/protein interaction [30], some tests were performed on samples exposed to plasma. Comparison has been done between untreated samples and samples pretreated with a pig plasma for 1 h at 37 °C.

Increased antibacterial effect resulting from colloidal silver was evidenced. However, it was found a new effect of reduction of the bacteria colonization obtained when lowering the implantation energy, leading to increased accessibility to the surface colloidal silver. This interpretation would in particular explain the high activity of silver implanted polymer. Studies at implantation energies below 10 keV, would then be of main interest for further improvements of the bactericidal activity. At the end, comparison between the efficiency of silver nanoparticles (at present study) and the efficiency of a continu-

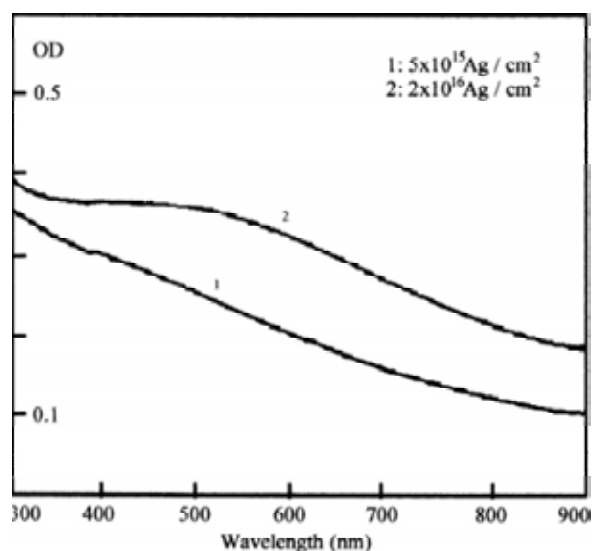


Fig. 23. Optical absorption spectra of PE films implanted silver ions. Adapted from [29].

ous metal film would be interesting, because of the known high activity of divided metals at the nanoscale [29].

4.3. Antibacterial activity against *E. coli* of implanted silver nanoparticles in silica

In our study the bactericidal properties of Ag-implanted silica glasses were investigated using *E. coli*. The size and position of the silver nanoparticles formed by ion implantation can be optimized by adjusting the implanted process parameters. All the implanted samples show antibacterial properties. The samples with 10 nm silver nanoparticle-enriched surfaces possess excellent antibacterial properties.

In order to create nanoparticles, silver ions are implanted into high-purity amorphous silica plates at room temperature by using a MEVVA ion source implanter. Fig. 24 displays the cross-section TEM bright-field images of the implanted samples. Formed silver nanoparticles are located near the surface.

The antibacterial activity was estimated for samples against *E. coli* by following a typical bactericidal experiment, the so-called antibacterial drop-test. *E. coli* O157 are used as the experimental bacteria and cultured on the culture medium at 37 °C overnight. Cultured bacteria are added in 10 mL saline solution to reach approximately the concentration of 10^8 CFU/mL. The samples are placed in sterilized Petri dishes. Then 100 μ L saline solution with bacteria at a concentration of 10^8 CFU/mL is added dropwise onto the surface of each deposited plate, and a piece of undeposited plate is

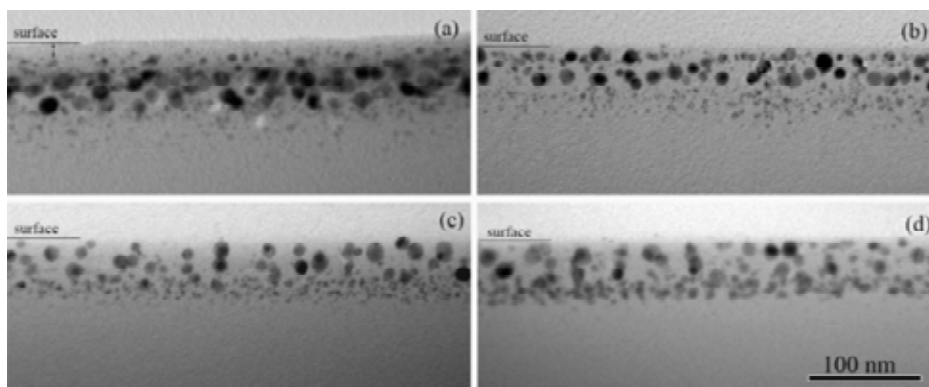


Fig. 24. Cross-section TEM images of Ag-implanted silica: a. - E1 (10^{17} ion/cm², 55 keV), b. - E2 (10^{17} ion/cm², 40 keV), c. - E3 (10^{17} ion/cm², 20 keV) and d. - E4 ($7 \cdot 10^{16}$ ion/cm², 20 keV).

used as a blank control. The surface of the sample is covered by an antistaling film. The samples are laid at ambient temperature for 24 h. After period the bacteria containing drops are washed from the surfaces of plates using 1 mL phosphate buffer solution (PBS) in the sterilized Petri dish. Then 100 uL of each bacteria suspension is dispersed on the culture medium. The number of surviving bacteria on the Petri dishes is counted after incubation overnight at 37 °C.

Fig. 25 shows the antibacterial experimental results. All the implanted samples show bactericidal characters. When the silver implantation dose is order of $1 \cdot 10^{17}$ ions/cm², E2 has superior antibacterial activity. Also E4 has the superior antibacterial property in the implanted-samples. Therefore, the implantation energy and dose reflect the relationship between the silver concentration and the bactericidal ratio.

The death of the bacteria is most probably caused by the adhesion of bacteria on the surface of the sample in contact with the silver atoms. The rougher surface can provide more opportunities for the contact between silver atoms and the bacteria. Therefore, the antibacterial property may be caused by a silver-enriched surface layer in the silica. The implantation energy (Fig. 24) and dose dependence reflect the relationship between the silver concentration and bactericidal ratio. When the silver concentration on the surface is higher, the bactericidal ratio is higher. Furthermore, the formed silver nanoparticles near the surface are all about 10 nm in size. Because of their small size, they present the great surface area which means great chances of contact with bacteria.

ACKNOWLEDGEMENTS

A.L.S. grateful to the Alexander von Humboldt Foundation and the DAAD (Germany). Also, this work

was partly supported by the Russian Foundation for Basic Research (Nos. 11-02-91341, 11-02-90420, 12-02-97029, 12-02-00528) and NIR KFU 13-56. T.K. was supported by the State Fund for Fundamental Researches of Ukraine (Nos. F40.2/019 and F52.2/003).

REFERENCES

- [1] P.T. Townsend, P.J. Chandler and L. Zhang, *Optical effects of ion implantation* (Cambridge Univ. Press, Cambridge, 1994).
- [2] A.L. Stepanov, *Ion-synthesis of silver nanoparticles and their optical properties* (Nova Sci. Publ., New York, 2010).

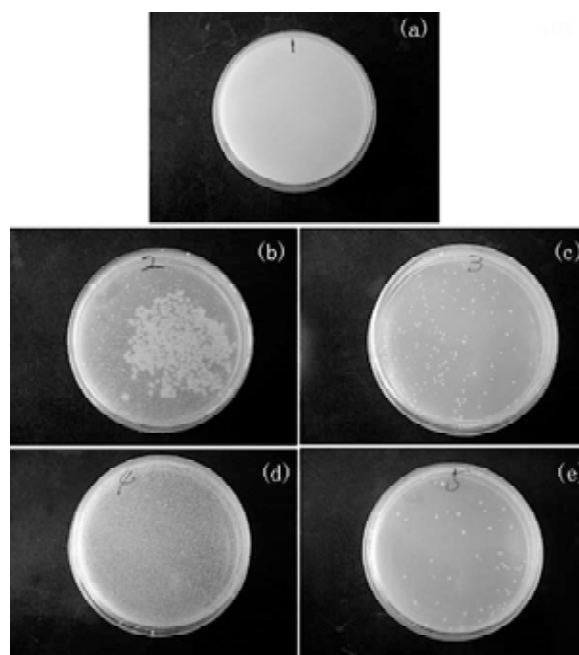


Fig. 25. Bacterial colonies: a. - E0 (virgin glass), b. - E1 (10^{17} ion/cm², 55 keV), c. - E2 (10^{17} ion/cm², 40 keV), d. - E3 (10^{17} ion/cm², 20 keV) and e. - E4 ($7 \cdot 10^{16}$ ion/cm², 20 keV).

- [3] A.L. Stepanov, S.N. Abdullin, V.Y. Petukhov, Y.N. Osin and I.B. Khaibullin // *Phil. Mag. B* **80** (2000) 23.
- [4] A.L. Stepanov and V.N. Popok // *Surf. Sci.* **566** (2004) 1250.
- [5] S. Deying, Y. Saito and S. Suganomata // *Jap. J. Appl. Phys.* **33** (1994) L966.
- [6] A.L. Stepanov, S.N. Abdullin, V.F. Valeev, Y.N. Osin, V.V. Bazarov and I.B. Khaibullin // *Mat. Res. Soc. Symp. Proc.* **392** (2003) 262.
- [7] A.L. Stepanov, D.E. Hole and P.D. Townsend // *J. Non.-Cryst. Sol.* **190** (1999) 275.
- [8] A.L. Stepanov, V.N. Popok, D.E. Hole and A.A. Bukharaev // *Phys. Solid State* **132** (2001) 2192.
- [9] H. Tsuji, H. Sugahara, Y. Gotoh and J. Ishikawa // *IEEE* **12** (2002) 705.
- [10] S.M. Gupta and M. Tripathi // *Chin. Sci. Bull.* **56** (2011) 1639.
- [11] K. Awazu, M. Fujimaki, C. Rickstuhl, J. Tominaga, H. Murakami, Y. Ohki, N. Yushida and T. Watanabe // *J. Am. Chem. Soc.* **130** (2008) 1676.
- [12] M. Logar, B. Jancar, S. Sturm and D. Suvorov // *Langmuir* **26** (2010) 12215.
- [13] P. Cristopher, D.B. Ingam and S. Linc // *J. Phys. Chem. C* **114** (2010) 9173.
- [14] F. Wu, X. Hu, J. Fan, E. Liu, T. Sun, L. Kang, W. Hou, C. Zhu and H. Liu // *Plasmonics* **12** (2012) 11468.
- [15] J. Yu, G. Dai and B. Huang // *J. Phys. Chem. C* **113** (2009) 16394.
- [16] M. Yu, Y. Wang, W. Sun and X. Yao // *Adv. Synth. Catal.* **354** (2012) 71.
- [17] M.A. Behnajady, N. Modirshahla, M. Shokri and B. Rad // *Global NEST J.* **10** (2008) 1.
- [18] A. Takai and P.V. Kamat // *ACS Nano* **5** (2011) 7369.
- [19] A.L. Linsebigler, G. Lu and J.T. Yates Jr. // *Chem. Rev.* **95** (1995) 735.
- [20] U. Kreibig and M. Vollmer, *Optical properties of metal clusters* (Springer: Berlin, 1995).
- [21] W.F. Zhang, Y.L. He, M.S. Zhang, Z. Yin and Q. Chen // *J. Phys. D: Appl. Phys.* **33** (2000) 912.
- [22] K.A. Willets and R.P. van Duyne // *Annu. Rev. Phys. Chem.* **58** (2007) 267.
- [23] X.H. Xiao, F. Ren, J.B. Wang, C. Liu and C.Z. Juang // *Mater. Lett.* **61** (2007) 4435.
- [24] M.D. Malinsky, K.L. Kelly, G.C. Schatz and R.P. van Dune // *J. Am. Chem. Soc.* **123** (2001) 1471.
- [25] H. Al-Ekabi and N. Serpone // *J. Phys. Chem.* **92** (1988) 5726.
- [26] T. Lu, Y. Qiao and X. Liu // *Interface Focus* **2** (2008) 325.
- [27] G. Taubes // *Science* **321** (2008) 356.
- [28] H. Cao, X. Liu, F. Meng and P.K. Chu // *Biomaterials* **32** (2011) 693.
- [29] J. Davenas, P. Thevenard, F. Philippe and M.N. Arnaud // *Biomol. Eng.* **19** (2002) 263.
- [30] R.L. Williams and D.F. Williams // *Biomaterials* **9** (1988) 206.